

An analytical template for gravitational-wave echoes: signal characterization and prospects of detection with current and future interferometers

Adriano Testa* and Paolo Pani†

Dipartimento di Fisica, “Sapienza” Università di Roma & Sezione INFN Roma1, Piazzale Aldo Moro 5, 00185, Roma, Italy

Gravitational-wave echoes in the post-merger ringdown phase are under intense scrutiny as probes of near-horizon quantum structures and as signatures of exotic states of matter in ultracompact stars. We present an analytical template that describes the ringdown and the echo signal for nonspinning objects in terms of two physical parameters: the reflectivity and the redshift at the surface of the object. We characterize the properties of the template and adopt it in a preliminary parameter estimation with current (aLIGO) and future (Cosmic Explorer, Einstein Telescope, LISA) gravitational-wave detectors. For fixed signal-to-noise ratio in the post-merger phase, the constraints on the model parameters depend only mildly on the details of the detector sensitivity curve, but depend strongly on the reflectivity. Our analysis suggests that it might be possible to detect or rule out Planckian corrections at the horizon scale for perfectly-reflecting ultracompact objects at 5σ confidence level with Advanced LIGO/Virgo. On the other hand, signal-to-noise ratios in the ringdown phase equal to ≈ 100 (as achievable with future interferometers) might allow us to probe near-horizon quantum structures with reflectivity $\gtrsim 30\%$ ($\gtrsim 85\%$) at 2σ (3σ) level.

I. INTRODUCTION

Gravitational-wave (GW) echoes in the post-merger GW signal from a binary coalescence might be a generic feature of quantum corrections at the horizon scale [1, 2], and might provide a smoking-gun signature of exotic compact objects (ECOs) and of exotic states of matter in ultracompact stars [3, 4] (for a review, see [5, 6]). In the last two years, tentative evidence for echoes in the combined LIGO/Virgo binary black-hole (BH) events have been reported [7, 8] with controversial results [9–12]. Recently, a tentative detection of echoes in the post-merger signal of neutron-star binary coalescence GW170817 [13] has been claimed at 4.2σ confidence level [14]. The stochastic background produced by “echoing remnants” [15] and spinning ECOs [16] has been also studied recently.

While model-independent [14] and burst [17] searches can be performed without knowing the details of the echo waveform, the possibility of extracting as much information as possible from post-merger events relies on one’s ability to model the signal accurately. Furthermore, using an accurate template is crucial for model selection and to discriminate the origin of the echoes in case of a detection. In the last year, there has been considerable progress in modeling the echo waveform [18–24], but the proposed approaches are sub-optimal, because either they are based on analytical templates not necessarily related to the physical properties and parameters of the remnant, or they rely on numerical waveforms which are inconvenient for direct searches through matched filters.

In this work, we take the first step to overcome these limitations by building an *analytical* template directly anchored to the physical properties of a given ECO

model. As we shall discuss, the template captures the rich phenomenology of the GW echo signal, including amplitude and frequency modulation, which arise from the physical origin of the echoes, namely radiation that bounces back and forth between the object and the photon-sphere [25], slowly leaking to infinity through wave tunneling [1, 2, 5, 6].

As an illustration and anticipation of our results, in Fig. 1 we compare the ringdown+echo signal derived below against the power spectral densities of current (aLIGO at design sensitivity [26]) and future (Einstein Telescope [27], Cosmic Explorer [28], LISA [29]) GW interferometers. Details on the template are provided in Sec. II. A preliminary parameter estimation using current and future GW detectors is performed in Sec. III. We conclude in Sec. IV with future prospects. Throughout this work, we use $G = c = 1$ units.

II. SETUP

As a first step, we focus on nonspinning models, the extension to spinning objects is underway. Our approach is based on the analytical approximation of perturbations of the Schwarzschild geometry in terms of the Pöschl-Teller potential [33, 34] and on the framework developed in Ref. [19], in which the echo signal is written in terms of a transfer function that reprocesses the BH response at the horizon. For the busy reader, our final template is provided in a ready-to-be-used form in Eq. (25) and in a supplemental MATHEMATICA[®] notebook [35].

A. An analytical template for GW echoes

We model the stationary ECO with a background geometry described, when $r > r_0$, by the Schwarzschild

* adriano.testa@roma1.infn.it

† paolo.pani@roma1.infn.it

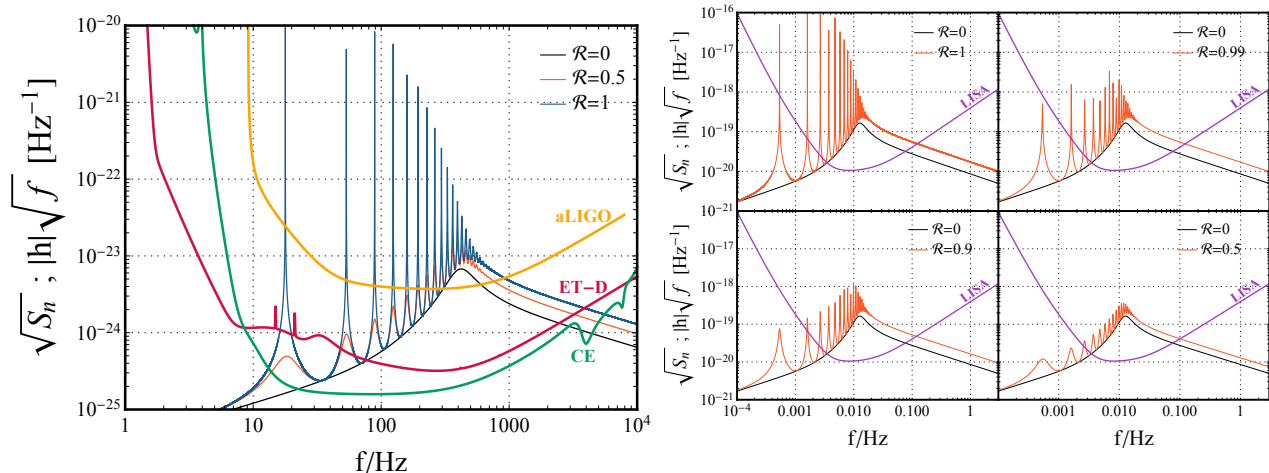


FIG. 1. Illustrative comparison between the ringdown+echo signal derived in this work and the power spectral densities of various interferometers as functions of the GW frequency f . Left panel: we considered an object with $M = 30M_{\odot}$, at a distance of $D = 400$ Mpc, with compactness parameter $d = 100M$ (roughly corresponding to near-horizon quantum corrections, see below) and various values of the reflectivity coefficient \mathcal{R} ($\mathcal{R} = 0$ corresponds to the pure BH ringdown template). The sensitivity curves refer to aLIGO with its anticipated design-sensitivity `ZERO_DET_high_P` configuration [26], Cosmic Explorer in the narrow band variant [30, 31], and Einstein Telescope in its ET-D configuration [32]. Right panels: the echo signal is compared to the recently proposed LISA’s noise spectral density [29]. We considered an object with $M = 10^6M_{\odot}$, at a distance of $D = 100$ Gpc (corresponding to cosmological redshift ≈ 10), and with $d = 100M$. Each small panel corresponds to a different value of \mathcal{R} . For simplicity in all panels we neglected corrections due to the geometry of the detector, sky averaging, and cosmological effects, and we assumed $\mathcal{A} \sim M/D$ for the amplitude of the ringdown signal. Details are given in the main text.

metric,

$$ds^2 = -Adt^2 + A^{-1}dr^2 + r^2d\Omega^2, \quad (1)$$

with $A(r) = 1 - 2M/r$, M and r_0 being the total mass and the radius of the object in Schwarzschild coordinates, respectively. At $r = r_0$, we assume the presence of a membrane, the properties of which are parametrized by a complex and (generically) frequency-dependent reflectivity coefficient [19, 36]. This model is well suited to describe near-horizon quantum structures (which belong to the *ClePhO* category introduced in Refs. [5, 6]).

After carrying out a Fourier transform and a spherical-harmonics decomposition, various classes of perturbations of the background metric are described by a master equation

$$\left[\frac{\partial^2}{\partial x^2} + \omega^2 - V_{sl}(r) \right] \tilde{\Psi}(\omega, x) = \tilde{S}(\omega, x), \quad (2)$$

where

$$x = r + 2M \log \left(\frac{r}{2M} - 1 \right) \quad (3)$$

defines¹ the tortoise coordinate x of the Schwarzschild metric, l is the multipolar index, s identifies the type of

the perturbation, and \tilde{S} is a source term. We assume that the surface of the object in tortoise coordinates is located near the would-be horizon at $x_0 = x(r_0) \ll -M$, as expected for near-horizon quantum corrections [1, 2, 5, 6]. The potential reads

$$V_{sl}(r) = A(r) \left(\frac{l(l+1)}{r^2} + \frac{1-s^2}{r} A'(r) \right), \quad (4)$$

where the prime denotes derivative with respect to the coordinate r . In the above potential, $l \geq s$ with $s = 0, 1$ for test Klein-Gordon and Maxwell fields, respectively, whereas $s = 2$ for axial gravitational perturbations (see Fig. 2). Also polar gravitational perturbations are described by Eq. (2), but in this case the potential reads

$$V_{2l}^P(r) = 2A \left[\frac{9M^3 + 9M^2r\Lambda + 3Mr^2\Lambda^2 + r^3\Lambda^2(1+\Lambda)}{r^3(3M+r\Lambda)^2} \right], \quad (5)$$

with $\Lambda = (l-1)(l+2)/2$ and $l \geq 2$. While axial and polar perturbations of a Schwarzschild BH are isospectral [37], this property is generically broken for ECOs [5, 6].

1. Transfer function

By using Green’s function techniques, Mark et al. [19] showed that the solution of Eq. (2) at infinity reads

¹ We note that our definition of x differs by a constant term $-2M \log 2$ relative to the one adopted in Ref. [19].

$\tilde{\Psi}(\omega, x \rightarrow \infty) \sim \tilde{Z}^+(\omega)e^{i\omega x}$, with

$$\tilde{Z}^+(\omega) = \tilde{Z}_{\text{BH}}^+(\omega) + \mathcal{K}(\omega)\tilde{Z}_{\text{BH}}^-(\omega). \quad (6)$$

In the above equation, $\tilde{Z}_{\text{BH}}^\pm$ are the responses of a Schwarzschild BH (at infinity and near the horizon, for the plus and minus signs, respectively) to the source \tilde{S} ,

$$\tilde{Z}_{\text{BH}}^\pm(\omega) = \int_{-\infty}^{+\infty} dx \frac{\tilde{S}\tilde{\Psi}_\mp}{W_{\text{BH}}}, \quad (7)$$

where $\tilde{\Psi}_\pm$ are the solutions of the homogeneous equation associated to Eq. (2) satisfying the boundary conditions

$$\tilde{\Psi}_\pm \rightarrow e^{\pm i\omega x} \quad \text{as } x \rightarrow \pm\infty, \quad (8)$$

and $W_{\text{BH}} = \frac{d\tilde{\Psi}_+}{dx}\tilde{\Psi}_- - \tilde{\Psi}_+\frac{d\tilde{\Psi}_-}{dx}$ is the Wronskian. The details of the ECO model are all contained in the transfer function

$$\mathcal{K}(\omega) = \frac{\mathcal{T}_{\text{BH}}\mathcal{R}e^{-2i\omega x_0}}{1 - \mathcal{R}_{\text{BH}}\mathcal{R}e^{-2i\omega x_0}}, \quad (9)$$

where $\mathcal{T}_{\text{BH}}(\omega)$ and $\mathcal{R}_{\text{BH}}(\omega)$ are the transmission and reflection amplitudes for waves coming from the *left* of the BH potential barrier [19, 37, 38], whereas $\mathcal{R}(\omega)$ is the reflection coefficient at the surface of the object, defined so that

$$\tilde{\Psi} \rightarrow e^{-i\omega(x-x_0)} + \mathcal{R}(\omega)e^{i\omega(x-x_0)}, \quad (10)$$

near the surface at $x \sim x_0$, with $|x_0| \gg M$. In Appendix A, we provide a heuristic derivation of Eq. (9) in terms of geometrical optics. The above equations are subject to the constraint that the time domain waveforms are real, which implies

$$\mathcal{K}(\omega) = \mathcal{K}^*(-\omega^*) \quad (11)$$

and analogous relations for the other quantities.

We notice that the signal in the frequency domain is written as a sum of the BH response plus an extra piece proportional to \mathcal{R} . The poles of this latter piece are the quasinormal modes (QNMs) of the ECO which, in general, differ from those of the BH. Since the BH QNMs scale with $1/M$ while the ECO QNMs scale with $1/d$, when $d \gg M$ the signal at small times is dominated by the poles of the BH (which are no longer QNMs since they do not satisfy the right boundary conditions, see discussion below).

2. Pöschl-Teller potential

The potential (4) [and (5)] can be approximated by the Pöschl-Teller potential [21, 33, 34]

$$V_{\text{PT}}(x) = \frac{V_0}{\cosh^2[\alpha(x-x_m)]}, \quad (12)$$

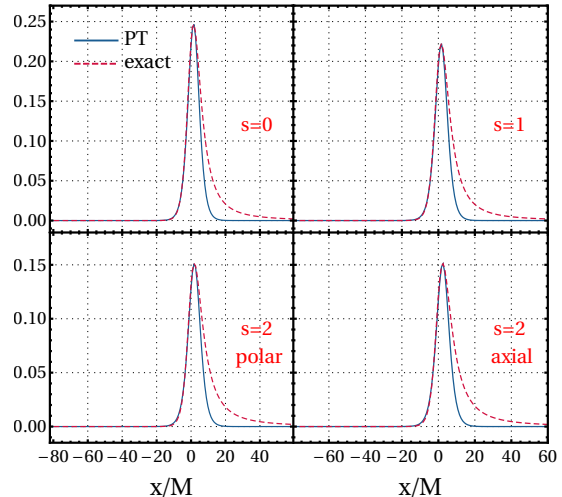


FIG. 2. Comparison between the exact potential governing perturbations in a Schwarzschild geometry (red dashed curve) and its approximation given by the Pöschl-Teller potential (PT, blue continuous curve), as explained in the text.

where α , V_0 and x_m are free parameters. We chose V_0 and x_m such that the position of the maximum and its value coincide with those of the corresponding V_{sl} . The remaining parameter α was found by imposing that the real part of the fundamental QNM of the Pöschl-Teller potential,

$$\omega_R = \sqrt{V_0 - \alpha^2/4}, \quad (13)$$

coincides with the exact one, as found numerically [39].

The values of α , V_0 and x_m obtained through this procedure for different classes of potentials are given in Table I. The Pöschl-Teller potential provides an excellent approximation on the left of the potential barrier and near the maximum (see Fig. 2), which are crucially the most relevant regions for our model. On the right of the potential barrier the behavior is different, since the Pöschl-Teller potential decays exponentially as $x \gg M$, whereas the exact potential decays as $\sim 1/x^2$. We have checked that this different behavior would affect only the reprocessing of very low frequency signals, but it is negligible for the first echoes, which are characterized by the reprocessing of the dominant QNMs with $\omega_R M \sim 1$.

Using the approximate potential, the homogeneous equation corresponding to Eq. (2) can be solved analytically. The general solution of the homogeneous problem, $\tilde{\Psi}_0$, can be expressed in terms of associated Legendre functions as

$$\tilde{\Psi}_0 = c_1 P_{\frac{i\omega}{\alpha}}^{\frac{i\omega}{\alpha}}(2\xi - 1) + c_2 Q_{\frac{i\omega}{\alpha}}^{\frac{i\omega}{\alpha}}(2\xi - 1), \quad (14)$$

where $\xi = [1 + e^{-2\alpha(x-x_m)}]^{-1}$ is a new variable. The integration constants c_1 and c_2 are related to the amplitudes of the transmitted and reflected waves and their

Potential	s	$\omega_R M$	$\omega_I M$	αM	$V_0 M^2$	x_m/M	$\Delta\omega_I/\omega_I$
scalar	0	0.4836	-0.09676	0.2298	0.2471	1.466	0.1876
electromagnetic	1	0.4576	-0.09500	0.2265	0.2222	1.614	0.1921
axial gravitational	2	0.3737	-0.08896	0.2159	0.1513	2.389	0.2136
polar gravitational	2	0.3737	-0.08896	0.2161	0.1513	1.901	0.2148

TABLE I. Numerical values of the fitting parameters of the Pöschl-Teller potential (12) used in this work to approximate the exact potential [see Fig. 2]. Scalar, electromagnetic and axial gravitational perturbations are described by the potential (4), whereas polar gravitational perturbations are described by the potential (5). We restrict to $l = 2$. As an indicator of the quality of the analytical approximation, in the last column we show the relative difference $\frac{\Delta\omega_I}{\omega_I}$ between the exact imaginary part of the frequency (shown in the fourth column) and that given by the Pöschl-Teller potential. The parameter x_m is expressed in terms of the tortoise coordinate defined in Eq. (3).

ratio is determined by the boundary conditions. With the analytical solution at hand, it is straightforward to obtain

$$\mathcal{T}_{\text{BH}} = -\frac{i}{\pi} \sinh\left(\frac{\pi\omega}{\alpha}\right) \Upsilon, \quad (15)$$

$$\mathcal{R}_{\text{BH}} = -\frac{1}{\pi} \cosh\left(\frac{\pi\omega_R}{\alpha}\right) \Upsilon e^{2i\omega x_m}, \quad (16)$$

where we defined

$$\Upsilon = \Gamma\left(\frac{1}{2} - i\frac{\omega + \omega_R}{\alpha}\right) \Gamma\left(\frac{1}{2} - i\frac{\omega - \omega_R}{\alpha}\right) \frac{\Gamma(1 + \frac{i\omega}{\alpha})}{\Gamma(1 - \frac{i\omega}{\alpha})}. \quad (17)$$

By replacing the above expressions in Eq. (9), we finally obtain

$$\mathcal{K}(\omega) = -i \frac{e^{2i\omega d} \mathcal{R}(\omega) \Upsilon \sinh\left(\frac{\pi\omega}{\alpha}\right)}{\pi + e^{2i\omega d} \mathcal{R}(\omega) \cosh\left(\frac{\pi\omega_R}{\alpha}\right) \Upsilon} e^{-2i\omega x_m}, \quad (18)$$

where we defined the width of the cavity² $d = x_m - x_0 > 0$ (recall that $x_0 < 0$ and $x_m > 0$), which is also related to the redshift at the surface, $z \sim e^{-d/M}$ when $d \gg M$. As we shall show later, the final signal depends only on the physical quantity d ; the dependence on x_m in Eq. (18) will disappear from the final result³.

In summary, for a given choice of $\mathcal{R}(\omega)$, the above relations yield an *analytical* approximation to the transfer function \mathcal{K} . In Appendix B, we compare some results for the approximate analytical expressions of \mathcal{T}_{BH} , \mathcal{R}_{BH} and \mathcal{K} , with their exact numerical counterparts as computed in Ref. [19].

² For ECOs with near-horizon quantum structures, one expects $d \sim nM |\log(l_P/M)|$, where l_P is the Planck length and $n \sim \mathcal{O}(1)$ depends on the model [2, 5, 6]. This gives $d/M \sim 100n$ roughly for both stellar-mass and supermassive objects. In this case, the redshift at the surface roughly reads $z \sim l_P/M$.

³ This must be the case and, in fact, it is possible to add a phase term in the definitions of the transfer function and of the BH response at the horizon so that x_m never appears in the equations. We chose not to do so in order to follow the notation of Ref. [19] more closely. Equivalently, in a coordinate system such that the maximum of the potential sits at the origin, all results would depend only on the physical quantity d .

3. Modeling the BH response

The inverse Fourier transform of the BH response $\tilde{Z}_{\text{BH}}^\pm(\omega)$ [see Eq. (7)] can be deformed in the complex frequency plane, yielding three contributions [39, 40]: (i) the high-frequency arcs that govern the prompt response; (ii) a sum-over-residues at the poles of the complex frequency plane (defined by $W_{\text{BH}} = 0$), which correspond to the QNMs and that dominate the signal at intermediate times; (iii) a branch cut on half of the imaginary axis, giving rise to late-time tails due to backscattering off the background curvature. The post-merger ringdown signal is very well approximated by the second contribution only, so that for most astrophysical applications the BH response at infinity can be written as a superposition of QNMs [39]. Considering for simplicity only the dominant mode, one gets

$$Z_{\text{BH}}^+(t) \sim \mathcal{A} \theta(t - t_0) \cos(\omega_R t + \phi) e^{-t/\tau}, \quad (19)$$

where the complex QNM frequency reads $\omega_R + i\omega_I$, $\tau = -1/\omega_I$, \mathcal{A} and ϕ are the amplitude and the phase, respectively, and t_0 parametrizes the starting time of the ringdown. In the above expression we have defined $\mathcal{A} = M \mathcal{A}_{lmn} S_{lmn}/D$, where M is the mass of the object, D is the distance of the source, \mathcal{A}_{lmn} is the amplitude of the BH QNM with quantum numbers $(l, m, n) = (2, 2, 0)$, and S_{lmn} are the corresponding spin-weighted spheroidal harmonics [41]. Given the BH responses in the time domain, the frequency-domain waveforms are obtained through the Fourier transform,

$$\tilde{Z}_{\text{BH}}^\pm(\omega) = \int_{-\infty}^{+\infty} \frac{dt}{\sqrt{2\pi}} Z_{\text{BH}}^\pm(t) e^{i\omega t}. \quad (20)$$

For the BH response at infinity, the Fourier transform yields

$$\tilde{Z}_{\text{BH}}^+(\omega) \sim \frac{\mathcal{A}}{2\sqrt{2\pi}} \left(\frac{\alpha_1}{\omega - \Omega_+} + \frac{\alpha_2}{\omega - \Omega_-} \right) e^{i\omega t_0}, \quad (21)$$

where $\Omega_\pm = \pm\omega_R + i\omega_I$, $\alpha_1 = -e^{-i(\phi+t_0\Omega_+)}$ and $\alpha_2 = -\alpha_1^*$.

It is worth noting that the complex poles are the same for Z_{BH}^+ and for Z_{BH}^- , since those are defined by $W_{\text{BH}} =$

0. This suggests that the BH response near the horizon might also be described by a superposition of QNMs⁴.

M	total mass of the object
\mathcal{A}	amplitude of the BH ringdown
ϕ	phase of the BH ringdown
t_0	starting time of the BH ringdown
d	width of the cavity ($z \sim e^{-d/M}$)
$\mathcal{R}(\omega)$	reflection coefficient at the surface

TABLE II. Parameters of the ringdown+echo template presented in this work. The first four parameters characterize the ordinary BH ringdown. The parameter z is the gravitational redshift at the ECO surface.

More in general, we are interested in perturbations produced by sources localized near the object, as expected for merger remnants. If we assume $\tilde{S}(\omega, x) = C(\omega)\delta(x - x_s)$, for any x_s well inside the cavity (where $V(x_s) \approx 0$), from Eq. (7) we can derive a relation between \tilde{Z}_{BH}^+ and \tilde{Z}_{BH}^- , namely:

$$\tilde{Z}_{\text{BH}}^- = e^{2i\omega x_s} (1 + \mathcal{R}_{\text{BH}} e^{-2i\omega x_s}) \frac{\tilde{Z}_{\text{BH}}^+}{\mathcal{T}_{\text{BH}}}. \quad (22)$$

Remarkably, the above relation is independent of the function $C(\omega)$ characterizing the source. Thus, \tilde{Z}_{BH}^- can be computed analytically using the expressions for \mathcal{R}_{BH} ,

$$\tilde{Z}^+(\omega) = \sqrt{\frac{\pi}{2}} \mathcal{A} \frac{e^{i(\omega - \omega_I)t_0} (1 + \mathcal{R}) \Gamma\left(1 - \frac{i\omega}{\alpha}\right) (\omega_R \sin(\omega_R t_0 + \phi) + i(\omega + i\omega_I) \cos(\omega_R t_0 + \phi)}{[(\omega + i\omega_I)^2 - \omega_R^2] [\pi \Gamma\left(1 - \frac{i\omega}{\alpha}\right) + e^{2id\omega} \mathcal{R} \cosh\left(\frac{\pi\omega_R}{\alpha}\right) \Gamma\left(\frac{1}{2} - i\frac{\omega + \omega_R}{\alpha}\right) \Gamma\left(\frac{1}{2} - i\frac{\omega - \omega_R}{\alpha}\right) \Gamma\left(1 + \frac{i\omega}{\alpha}\right)]}. \quad (25)$$

The above result is valid for any type of perturbation, provided the parameters α and V_0 (or, equivalently, α

\mathcal{T}_{BH} and \tilde{Z}_{BH}^+ derived above. As expected, the quantity $\mathcal{K}\tilde{Z}_{\text{BH}}^-$ [appearing in Eq. (6)] is independent of x_m and depends only on the physical width of the cavity d .

An expression similar to Eq. (22) can be obtained for a source localized⁵ at any point x_s by using the explicit form of Eq. (14) [42]. The generic expression is given in Appendix C. In what follows we will consider a source localized near the surface, $x_s \approx x_0$, which should provide a model for post-merger excitations.

4. Ringdown+echo template

Putting together all the ingredients previously derived, the final expression of the full ECO response reads

$$\tilde{Z}^+(\omega) = Z_{\text{BH}}^+(\omega) \left[1 + \mathcal{R} \frac{\pi - e^{2i\omega d} \Upsilon \cosh\left(\frac{\pi\omega_R}{\alpha}\right)}{\pi + e^{2i\omega d} \mathcal{R} \Upsilon \cosh\left(\frac{\pi\omega_R}{\alpha}\right)} \right], \quad (24)$$

where Υ is defined in Eq. (17). In this form, the signal is written as the reprocessing of a generic BH response $Z_{\text{BH}}^+(\omega)$. Note that the BH response $Z_{\text{BH}}^+(\omega)$ might not necessarily be restricted to a ringdown signal in the frequency domain. In general, if the remnant is an ECO, one might expect that the post-merger phase can be obtained through the reprocessing of the ringdown part *and* of the late-merger phase, since already during the formation of the final ECO radiation might be trapped by an effective photon-sphere.

If instead we model the BH response $Z_{\text{BH}}^+(\omega)$ through a single ringdown [Eq. (21)], the explicit final form of the ringdown+echo signal reads

and ω_R) are chosen appropriately (see Table I). In the next section we will use Eq. (25) for polar gravitational perturbations.

For a linearly polarized wave, our template is defined by 4 real parameters (\mathcal{A} , ϕ , t_0 and d) plus the mass (which sets the scale for the other dimensionful quantities) and the complex function $\mathcal{R}(\omega)$ that is model dependent (see Table II). Clearly, for $\mathcal{R} = 0$ one recovers a single-mode BH ringdown template in the frequency domain. The echo contribution is fully determined only in terms of d and $\mathcal{R}(\omega)$ once the parameters of the ordinary ringdown are known. If two polarizations are included, the number of real parameters increases to 7 (\mathcal{A}_+ , \mathcal{A}_\times , ϕ_+ , ϕ_\times , t_0 , M , d), plus the function $\mathcal{R}(\omega)$.

The templates (24) and (25) are also publicly available in a ready-to-be-used supplemental MATHEMATICA[®] notebook [35].

⁴ Note that, since the Pöschl-Teller potential is symmetric under reflections around its maximum, within our approximation the BH response near the horizon would be equivalent to the response at infinity provided the source term in Eq. (7) has the same symmetry of the potential. However, this is generally not the case.

⁵ Another particular case is when the source is localized well outside the light ring ($x_s \gg M$). In this case we obtain

$$\tilde{Z}_{\text{BH}}^+ = e^{-2i\omega x_s} (1 + \hat{\mathcal{R}}_{\text{BH}} e^{2i\omega x_s}) \frac{\tilde{Z}_{\text{BH}}^-}{\hat{\mathcal{T}}_{\text{BH}}}, \quad (23)$$

where $\hat{\mathcal{R}}_{\text{BH}}$ and $\hat{\mathcal{T}}_{\text{BH}}$ are respectively the reflection and transmission coefficients for the scattering of left-moving waves from infinity. Note that, since the Pöschl-Teller potential is symmetric around its maximum, within our framework these coefficients coincide with \mathcal{R}_{BH} and \mathcal{T}_{BH} , respectively, modulo a phase difference.

B. Properties of the template

1. Time-domain echo signal

The time-domain signal can be simply computed through an inverse Fourier transform,

$$h(t) = \frac{1}{\sqrt{2\pi}} \int_{-\infty}^{+\infty} d\omega \tilde{Z}^+(\omega) e^{-i\omega t}. \quad (26)$$

In Figs. 3 and 4, we present a representative slideshow of our template for different values of d , $\mathcal{R}(\omega)$, and for scalar and polar gravitational perturbations, respectively. For simplicity, we consider $\mathcal{R}(\omega) = \text{const}$. The time-domain waveform contains all the features previously reported for the echo signal, in particular amplitude and frequency modulation [1, 2, 5, 6], and phase inversion [7, 24] of each echo relative to the previous one due to the reflective boundary conditions.

2. Decay of the echo amplitude in time

Several qualitative features of the waveforms can be understood with a simple geometrical-optics toy model presented in Appendix A. From this model, we expect the complex amplitude of each echo (in the frequency domain) relative to the previous one to be suppressed by a frequency-dependent factor $\mathcal{R}\mathcal{R}_{\text{BH}}$, where we dropped the phase term $e^{-2i\omega d}$ that accounts for the time delay between the two. The first echo has already a factor $\mathcal{R}_{\text{BH}}(\omega)$, which is essentially a low-pass filter. As shown in Fig. 9, $\mathcal{R}_{\text{BH}}(\omega) \approx 0$ for $\omega \gtrsim \omega_R$, whereas $|\mathcal{R}_{\text{BH}}(\omega)| \approx 1$ for $\omega \lesssim \omega_R$. Thus, for frequencies $\omega < \omega_R$, we expect that the amplitude of the echoes in the time domain should decrease as

$$A_{\text{echo}}(t) \propto |\mathcal{R}\mathcal{R}_{\text{BH}}|^{\frac{t}{2d}} \approx |\mathcal{R}|^{\frac{t}{2d}}. \quad (27)$$

As shown in Fig. 5, Eq. (27) agrees almost perfectly with our numerical results in the time domain (we expect the small departure of the line from the data to be a consequence of the fact that $|\mathcal{R}_{\text{BH}}|$ is not exactly constant).

3. Phase inversion of subsequent echoes

The phase inversion between subsequent echoes shown in Figs. 3 and 4 can be understood by considering the extra factor $\mathcal{R}\mathcal{R}_{\text{BH}}$ each echo has with respect to the previous one. When \mathcal{R} is real and positive, the phase is set by $\mathcal{R}_{\text{BH}}(\omega)$. Since $\mathcal{R}_{\text{BH}}(\omega \sim 0) \approx -1$ for low-frequency signals (which are the only ones that survive the first filtering by \mathcal{R}_{BH}), the n -th echo has a phase factor $[\mathcal{R}_{\text{BH}}(\omega \sim 0)]^n \approx (-1)^n$. If the ECO is a wormhole, there is no phase inversion because in this case $\mathcal{R} = \mathcal{R}_{\text{BH}} e^{-2i\omega x_0}$ [19], so that $\mathcal{R}\mathcal{R}_{\text{BH}} = \mathcal{R}_{\text{BH}}^2$, where again we dropped the time-shifting phase. Likewise, if

\mathcal{R} is real and negative, the n -th echo has a phase factor $[\mathcal{R}\mathcal{R}_{\text{BH}}]^n \approx 1$ for any n , so also in this case there is no phase inversion. Although not shown in Figs. 3 and 4, we have checked that all these properties are reproduced by the time-domain templates. Additional waveforms are provided online [35].

4. Dependence on the location of the source

From the geometrical optics analogy of Appendix A, we expect that, for a source located inside the cavity at some $x_s = x_0 + \ell$, the effect of the surface will appear only after a (coordinate-time) delay of 2ℓ with respect to the RD, because of the extra time it takes for the left-going perturbation to reach the surface and come back. Since the latter has a relative amplitude \mathcal{R} , the amplitude of the prompt signal is $\approx \mathcal{A}(1 + \mathcal{R}e^{2i\omega\ell})$. If $x_s \approx x_0$ (i.e., $\ell \approx 0$), there is no delay between the proper ringdown signal and the first reflection. This is consistent with the behavior of the signal shown in Fig. 1: the full response at high frequencies (i.e., those which are not reflected by the potential but only by the surface) differs from the BH ringdown by a relative factor $1 + \mathcal{R}$. Note that, if $x_s = x_0$, in the Dirichlet case ($\mathcal{R} = -1$) the prompt signal and the reflected one interfere with opposite phase and the signal vanishes, as clear from Eq. (25).

When the source is located outside the light ring [and consequently one needs to use Eq. (23)], the frequency content of the ECO response at infinity changes significantly. Indeed, in this case the low-frequency content of an incident packet would not be able to probe the cavity and would be reflected regardless of the nature of the object and of the boundary conditions at x_0 . On the other hand, the very high frequency component should pass through the light ring barrier unmodified and be reflected only by the ECO surface. The frequency-domain signal for a source localized at a generic location x_s is given in Appendix C.

5. Energy of echo signal

Finally, let us discuss the energy contained in the ringdown+echo signal. Because of partial reflection, the energy contained in the full signal is always larger than that of the ringdown itself. This is shown in Fig. 6, where we plot the energy

$$E \propto \int_0^\infty d\omega \omega^2 |\hat{Z}^+|^2, \quad (28)$$

normalized by the one corresponding to the ringdown alone, $E_{\text{RD}} = E(\mathcal{R} = 0)$, as a function of the reflectivity \mathcal{R} . In the above equation, \hat{Z}^+ is the frequency-domain full response obtained by using the Fourier transform of

$$\mathcal{Z}_{\text{BH}}^+(t) \sim \mathcal{A} \cos(\omega_R t + \phi) e^{-|t|/\tau}, \quad (29)$$

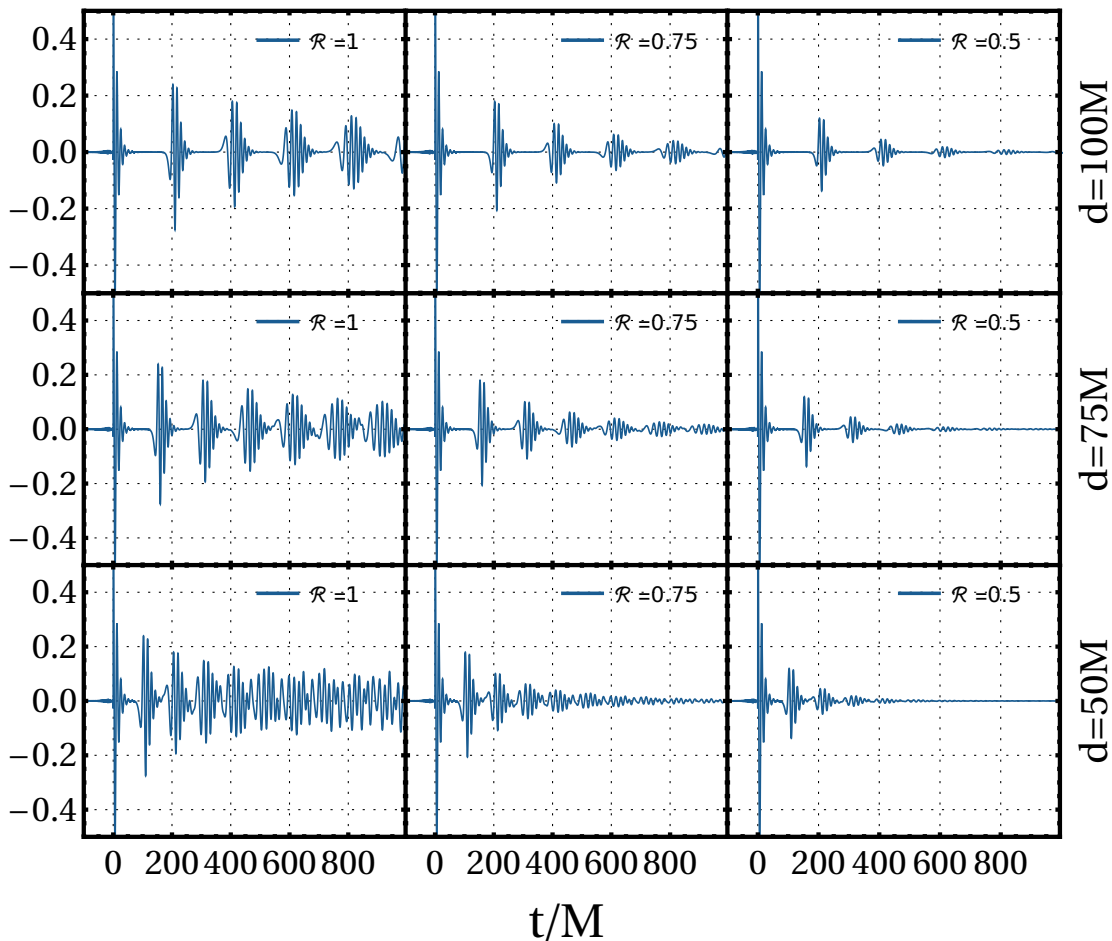


FIG. 3. Examples of the ringdown+echo template in the time domain for different values of d and $\mathcal{R}(\omega) = \text{const}$ and for scalar perturbations. From top to bottom: $d = 100M$, $d = 75M$, $d = 50M$; from left to right: $\mathcal{R} = 1$, $\mathcal{R} = 0.75$, $\mathcal{R} = 0.5$. The waveform is normalized to its peak value during the ringdown (not shown in the range of the y axis to better visualize the subsequent echoes).

rather than using Eq. (19). This is the prescription used in Ref. [43] to compute the ringdown energy, and it circumvents the fact that the Heaviside function in Eq. (19) produces a spurious high-frequency behaviour of the energy flux, leading to infinite energy in the ringdown signal. With the above prescription, the energy defined in Eq. (28) is finite and reduces to the result of Ref. [43] for the BH ringdown when $\mathcal{R} = 0$.

As shown in Fig. 6, the energy contained in the ringdown+echo signal depends strongly on \mathcal{R} and can be ≈ 38 times larger than that of the ringdown alone when $\mathcal{R} \rightarrow 1$ (the exact number depends also on t_0 and ϕ). This is due to the resonances⁶ corresponding to the low-

frequency QNMs of the ECO, that can be excited with large amplitude [see Fig. 1]. At high frequency there are no resonances, but the energy flux $dE/d\omega$ is larger than the ringdown energy flux by a factor $(1 + \mathcal{R})^2$, in agreement with our previous discussion.

and high. However, the most narrow resonances contribute little to the total energy. For example, in the extreme case $\mathcal{R} = 1$ and $d = 100M$, the integral (28) converges numerically when using fixed frequency steps $\Delta f \approx 0.001/M$ or smaller. This suggests that not resolving all resonances in the signal might not lead to a significant loss in the SNR. We are grateful to Jing Ren, whose comment prompted this analysis.

⁶ As shown in Fig. 1, when $\mathcal{R} = 1$ the resonances are very narrow

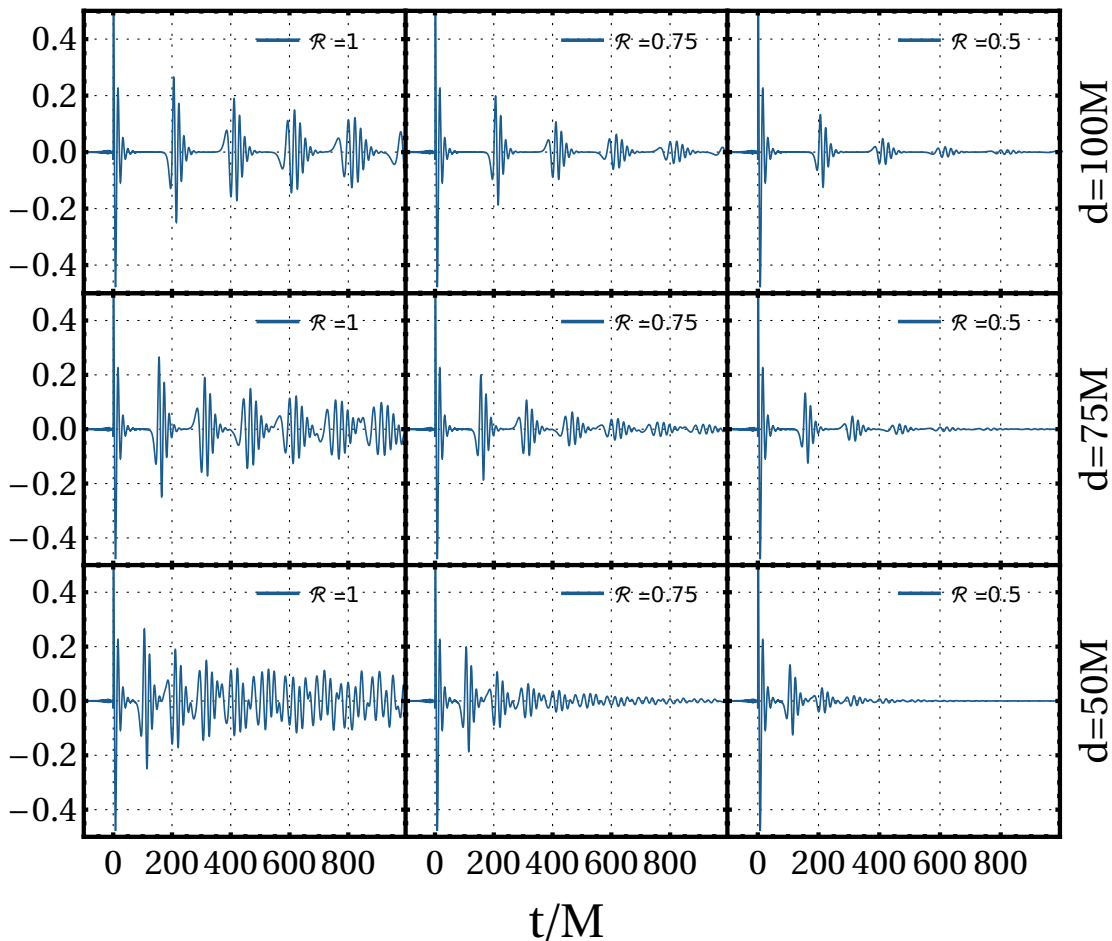


FIG. 4. Same as in Fig. 3, but for polar gravitational perturbations.

6. Connections with the QNMs

The final expression (24) also helps clarifying why the “prompt” ringdown signal of an ECO is identical to that of a BH even if the BH QNMs are not part of the QNM spectrum of an ECO [1, 44]. While this fact is easy to understand in the time domain (in terms of time needed for the perturbation to probe the boundaries [1]), it is less obvious in the frequency domain.

The crucial point is that the BH QNMs are still poles of the ECO full response, $\tilde{Z}^+(\omega)$, in the complex frequency plane, even if they are not part of the ECO QNM spectrum. Indeed, Eq. (24) contains two types of complex poles: those associated with $\tilde{Z}_{\text{BH}}^+(\omega)$ which are the standard BH QNMs (but do not appear in the ECO QNM spectrum), and those associated with the poles of the transfer function \mathcal{K} , which correspond to the ECO QNMs. The late-time signal is dominated by the second type of poles, since the latter have lower frequency

than the BH QNMs. On the other hand, the prompt ringdown is dominated by the first type of poles, i.e. by the dominant QNMs of the corresponding BH spacetime.

III. PROJECTED CONSTRAINTS ON ECOS

In this section we use the template previously derived [Eq. (25)] for a preliminary parameter estimation of the ECO properties using current and future GW detectors. We shall focus on polar gravitational perturbations with $l = 2$, which are typically the dominant ones.

As already illustrated in Fig. 1, the ringdown+echo signal displays sharp peaks which originate from the resonances of the transfer function \mathcal{K} [see Fig. 9] and correspond to the long-lived QNMs of the ECO. Indeed, they are very well described by the harmonics of normal modes in a cavity of width d [see Eq. (B2)] (with a finite resonance width given by the small imaginary

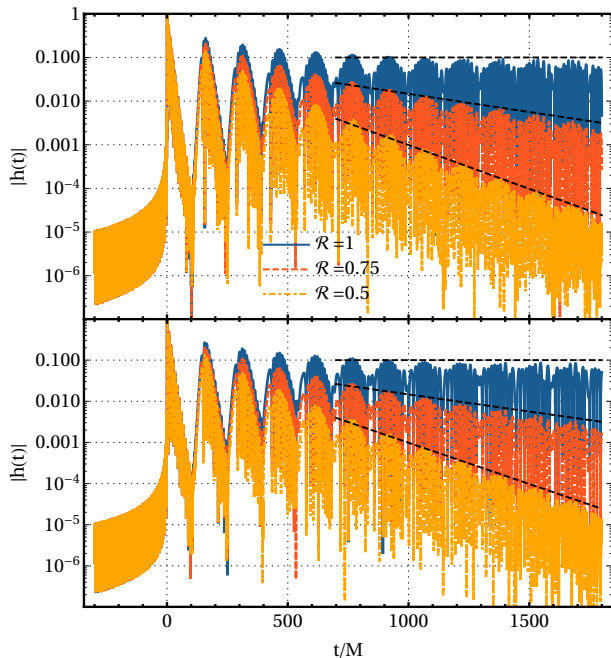


FIG. 5. Normalized absolute value of $h(t)$ for scalar (top panel) and polar gravitational (bottom panel) echo template. Continuous black lines show the slope $|h(t)| \sim 0.1|\mathcal{R}|^{t/(2d)}$, see Eq. (27). We set $d = 75M$ and considered $\mathcal{R} = (1, 0.75, 0.5)$; different choices of the parameters give similar results.

part of the mode [25, 45]) and their frequency separation is $\Delta\omega \propto 1/(d)$. The relative amplitude of each resonance in the signal depends on the source, and the dominant modes are not necessarily the fundamental harmonics [19, 21].

Although only indicative, Fig. 1 already shows two important features. First, the amplitude of the echo signal in the frequency domain can be *larger* than that of the ringdown itself. This explains the aforementioned energy content of the echo signal with respect to the ordinary ringdown (Fig. 6) and suggests that GW echoes might be detectable even when the ringdown is not (we note that this feature is in agreement with some claims of Refs. [7, 8, 14]). Second, as shown in the right panels of Fig. 1, the amplitude of the echo signal depends strongly on the value of \mathcal{R} and changes by several orders of magnitude between $\mathcal{R} = 0.5$ and $\mathcal{R} = 1$ (and even more for smaller values of \mathcal{R}). This suggests that the detectability of (or the constraints on) echoes will strongly depend on \mathcal{R} and would be much more feasible when $\mathcal{R} \approx 1$. Below we shall quantify this expectation.

A. Fisher analysis

For simplicity, we employ a Fisher analysis, which is accurate at large signal-to-noise ratios (SNRs) (see, e.g.,

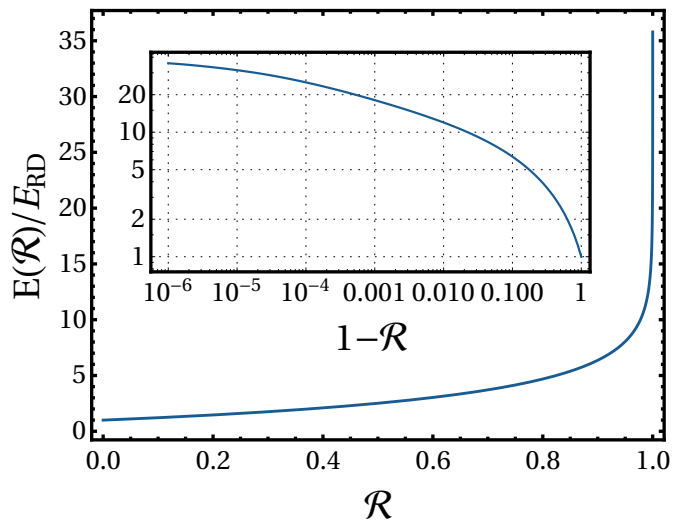


FIG. 6. Total energy contained in the ringdown+echo signal normalized by that of the ringdown alone as a function of \mathcal{R} . The inset shows the same quantity as a function of $1 - \mathcal{R}$ in a logarithmic scale. Note that the energy is much larger than the ringdown energy when $\mathcal{R} \rightarrow 1$. We set $t_0 = 0 = \phi$ and $d = 100M$; the result is independent of d in the large- d limit.

Ref. [46]). We shall assume that the signal is linearly polarized; including two polarizations is a straightforward extension.

Furthermore, since our ringdown+echo template was built for nonspinning ECOs, in principle we should also neglect the spin of the final object. However, since the statistical errors obtained from the Fisher matrix depend on the number of parameters, it is more realistic to assume that the template depends on the spin (through ω_R and ω_I , taken to be those of a Kerr BH rather than of a Schwarzschild BH) and to perform the Fisher analysis by injecting a vanishing value of the spin. This procedure introduces some systematics, since we are ignoring the remaining spin dependence of the echo template. Nonetheless, it should provide a more reliable order-of-magnitude estimate of the statistical errors on the ECO parameters in the spinning case.

The Fisher matrix Γ of a template $\tilde{h}(f)$ for a detector with noise spectral density $S_n(f)$ is defined as

$$\Gamma_{ij} = (\partial_i \tilde{h}, \partial_j \tilde{h}) = 4 \Re \int_0^\infty \frac{\partial_i \tilde{h}^*(f) \partial_j \tilde{h}(f)}{S_n(f)} df, \quad (30)$$

where $i, j = 1, \dots, N$, with N being the number of parameters in the template, and $f = \omega/(2\pi)$ is the GW frequency. The SNR ρ is defined as

$$\rho^2 = 4 \int_0^\infty \frac{\tilde{h}^*(f) \tilde{h}(f)}{S_n(f)} df. \quad (31)$$

The inverse of the Fisher matrix, Σ^{ab} , is the covariance matrix of the errors on the template's parameters: $\sigma_i = \sqrt{\Sigma^{ii}}$ gives the statistical error associated with the measurement of i -th parameter.

We note that, to the leading order in the large SNR limit, the statistical errors estimated through the Fisher matrix are independent of the systematic errors arising from approximating the true signal with an imperfect theoretical template [47].

1. Validation of the method: BH ringdown

As a check of our computation, we have reproduced the results of the BH ringdown analysis performed in Ref. [41]. This can be achieved by neglecting the echo part of our template, i.e. by setting $\mathcal{R} = 0$ or simply considering only the first term in Eq. (6).

We have first reproduced the analytical results presented in Appendix B of Ref. [41] for what concerns the statistical errors on the parameters of the ringdown waveform. We have then derived the same results through a numerical integration of Eq. (30). Note that Ref. [41] adopted a δ -approximation (i.e., white noise, $S_n(f) = \text{const}$), which is equivalent to consider the signal as monochromatic. In this limit, the quantity $\rho\sigma_i$ is by construction independent of the detector sensitivity. As a further check, we have relaxed the δ -approximation and repeated the analysis using the recently proposed LISA's noise spectral density [29], obtaining similar results.

2. Analysis for GW echoes

After having validated our scheme, we computed numerically the Fisher matrix (30) with the template (25) using the sensitivity curves presented in Fig. 1 for current and future detectors. As previously discussed, for linearly polarized waves the template contains 5 ringdown parameters (mass, spin, phase, amplitude, and starting time), and two ECO parameters (the frequency-dependent reflection coefficient $\mathcal{R}(\omega)$ and the width of the cavity d) which fully characterize the echoes. The parameter d is directly related to physical quantities, such as the compactness of the ECO or the redshift at the surface.

B. Results

Our main results for the statistical errors on the ECO parameters are shown in Fig. 7. In the large SNR limit, the errors scale as $1/\rho$ so we present the quantity $\rho\Delta\mathcal{R}/\mathcal{R}$ (left panel) and $\rho\Delta(d/M)/(d/M)$ (right panel⁷). Figure 7 shows a number of interesting features:

- The relative errors are almost independent of the sensitivity curve of the detector and only depend

on the SNR. This suggests that the parameter estimation of echoes will be only mildly sensitive to the details of future detectors. Obviously, future interferometers on Earth and in space will allow for very high SNR in the post-merger phase ($\rho \approx 100$ for ET/Cosmic Explorer, and possibly even larger for LISA), which will put more stringent constraints on the ECO parameters. This mild dependence of the relative errors on the sensitivity curve is valid for signals located near the minimum of the sensitivity curve, as those adopted in Fig. 7. Less optimal choices of the injected parameters would give a more pronounced (although anyway small) dependence, which is due to the different behavior of the various sensitivity curves at low/high frequencies.

- Although Fig. 7 was obtained by injecting the value $d = 100M$, the statistical absolute errors on \mathcal{R} and d do not depend on the injected value of d in the $d \rightarrow \infty$ limit. We give an analytical explanation of this seemingly counter-intuitive property in Appendix D. The statistical errors for $d = 100M$ are very similar to those for $d = 50M$ and saturate for larger values of d/M . Overall, our analysis suggests that the detectability of the echoes is independent of d in the large- d limit (i.e., for ultracompact objects).
- A further important feature is the strong dependence of the relative errors on the value of the reflection coefficient \mathcal{R} . In particular, the relative errors for $\mathcal{R} = 1$ are smaller than those for $\mathcal{R} \approx 0.5$ roughly by 4 orders of magnitude. The reason for this is related to what is shown in Figs. 1 and 6: the amplitude of individual echoes and the total energy of the signal depend strongly on the reflection coefficient. This feature suggests that it should be relatively straightforward to rule out or detect models with $\mathcal{R} \approx 1$, whereas it is increasingly more difficult to constrain models with smaller values of \mathcal{R} .

As an example, let us consider the extremal case $\mathcal{R} = 1$. Although this case is ruled out by the ergoregion instability [36, 48] and by the absence of GW stochastic background in LIGO O1 [16], it is interesting to explore the level of constraints achievable in this case. For a reference event with $M = 30M_\odot$ and $d > 50M$ with aLIGO, we obtain

$$\frac{\Delta\mathcal{R}}{\mathcal{R}} \approx 5 \times 10^{-8} \left(\frac{8}{\rho_{\text{ringdown}}} \right) \quad \text{for } \mathcal{R} = 1, \quad (32)$$

where, as a reference, we normalized ρ such that the value of the SNR *in the ringdown phase only*⁸ is that of

⁷ We adopted dimensionless parameters to define the Fisher matrix, in particular M/M_\odot and d/M . The statistical error on d can be easily obtained from the full covariance matrix.

⁸ When $\mathcal{R} \approx 1$, the SNR in the ringdown phase can differ significantly from the SNR in the whole post-merger phase, see Fig. 6. For $\mathcal{R} = 1$, and for the parameters considered in Eq. (32), the total SNR is $\rho \approx 18\rho_{\text{ringdown}}$.

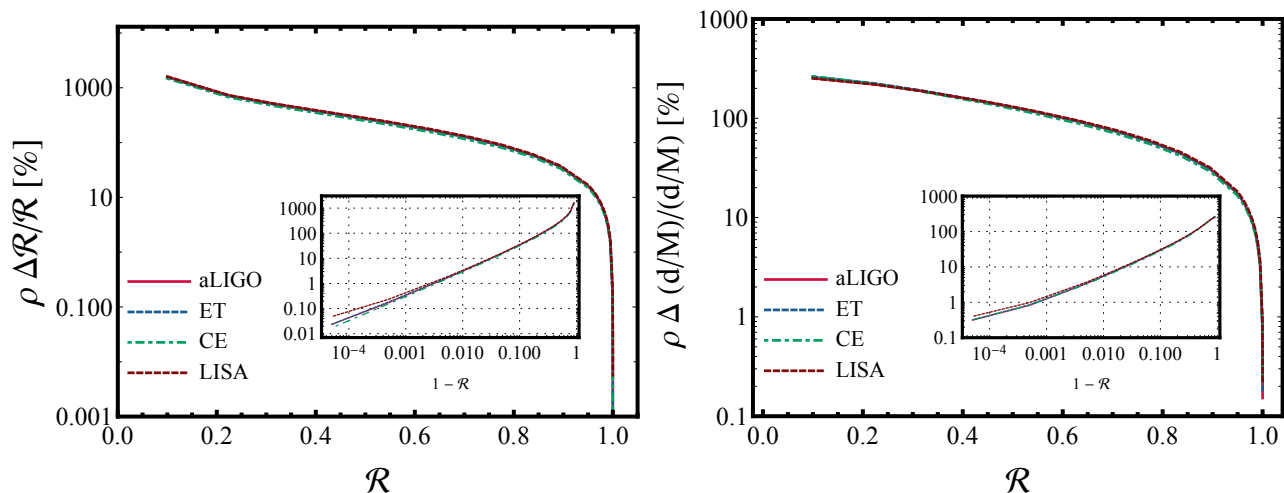


FIG. 7. Left panel: relative (percentage) error on the reflection coefficient, $\Delta\mathcal{R}/\mathcal{R}$, as a function of \mathcal{R} . The inset shows the same quantity as a function of $1 - \mathcal{R}$ in a logarithmic scale. Right panel: same as in the left panel but for the width of the cavity, $\Delta(d/M)/(d/M)$. For simplicity, we assumed that \mathcal{R} is real and positive. In both panels we considered $M = 30M_\odot$ for ground-based detectors and $M = 10^6M_\odot$ for LISA. We assume $d = 100M$ but the errors are independent of d in the large- d limit, see Appendix D.

GW150914 [49]. This suggests that this model could be detected or ruled out compared to the BH case ($\mathcal{R} = 0$) at more than 5σ confidence level with aLIGO/Virgo.

Figure 7 also shows a strong dependence of $\Delta\mathcal{R}/\mathcal{R}$ when $\mathcal{R} < 1$. It is therefore interesting to calculate the SNR necessary to discriminate a partially-absorbing ECO from a BH on the basis of a measurement of \mathcal{R} at some confidence level. Clearly, if $\Delta\mathcal{R}/\mathcal{R} > 100\%$, the measurement would be compatible with the BH case ($\mathcal{R} = 0$). On the other hand, if $\Delta\mathcal{R}/\mathcal{R} < (4.5, 0.27, 0.007, 0.00006)\%$, one might be able (by performing a more sophisticated analysis than the one presented here) to detect or rule out a given model at $(2, 3, 4, 5)\sigma$ confidence level, respectively.

The result of this preliminary analysis is shown in Fig. 8, where we present the exclusion plot for the parameter \mathcal{R} as a function of the SNR in the ringdown phase. Shaded areas represent regions which can be excluded at some given confidence level. Obviously, larger SNRs would allow to probe values of \mathcal{R} close to the BH limit, $\mathcal{R} \approx 0$. The level of the constraints strongly depends on the confidence level. For example, SNR ≈ 100 in the ringdown would allow to distinguish ECOs with $\mathcal{R} \gtrsim 0.3$ from BHs at 2σ confidence level, but a 3σ detection would require $\mathcal{R} \gtrsim 0.85$. The reason for this is again related to the strong dependence of the echo signal on \mathcal{R} (see Figs. 1 and 6).

Finally, the red marker in Fig. 8 corresponds to a detection at $\rho = 8$ in the ringdown phase (such as GW150914 [49]) and an ECO with reflectivity $\mathcal{R} = 0.9$. These are roughly the values of the tentative detection claimed in Ref. [7] at $(1.6 \div 2)\sigma$ level (but see also Refs. [8–12]). Although our analysis is preliminary, it is interesting to note that our results are not in tension with the

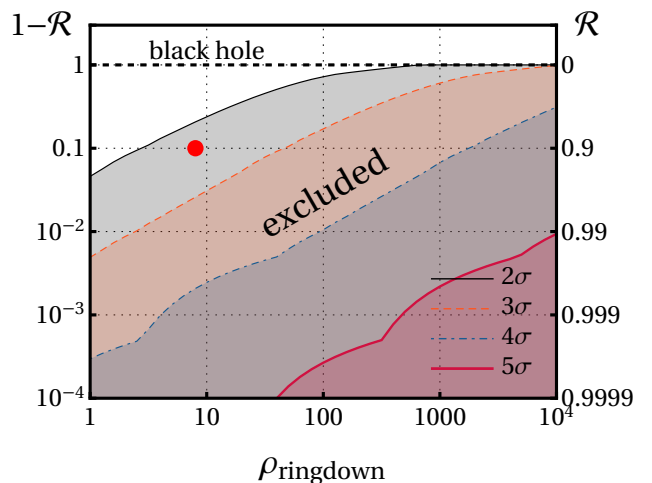


FIG. 8. Projected exclusion plot for the ECO reflectivity \mathcal{R} as a function of the SNR in the ringdown phase and at different σ confidence levels. Shaded areas represent regions that can be excluded at a given confidence level. This plot is based on Fig. 7 and assumes $d \gg M$ and $M = 30M_\odot$ ($M = 10^6M_\odot$) for ground- (space-) based detectors. The red marker corresponds to $\rho_{\text{ringdown}} = 8$ and $\mathcal{R} = 0.9$, which is the value claimed in Ref. [7] at $(1.6 \div 2)\sigma$ level.

claim of Ref. [7], since Fig. 8 suggests that an ECO with $\mathcal{R} = 0.9$ could be detected at $\lesssim 2.5\sigma$ confidence level through an event with $\rho_{\text{ringdown}} \approx 8$. On the other hand, the Fisher analysis only gives an estimate of the statistical errors in the large-SNR regime, but it would also be in agreement with a negative search. We consider the results shown in Fig. 8 as merely indicative that interesting constraints on (or detection of) quantum-dressed ECOs

are within reach current and, especially, future detectors. Indeed, Fig. 8 shows that to confirm the putative detection of Ref. [7] at 3σ (4σ) level would require a single-event detection with $\rho_{\text{ringdown}} \approx 50$ ($\rho_{\text{ringdown}} \approx 1800$).

IV. DISCUSSION AND OUTLOOK

We have presented an analytical template that describes the ringdown and subsequent echo signal of a ultracompact horizonless object motivated by putative near-horizon quantum structures. This template depends on the physical parameters of the echoing remnant, such as the reflection coefficient \mathcal{R} and the redshift at the surface of the object. This study is the first step in the development of an accurate template to be used in direct searches for GW echoes using matched filters and in parameter estimation.

We have characterized some of the features of the template, which are anchored to the physical properties of the ECO model. The time-domain waveform contains all features previously reported for the echo signal, namely amplitude and frequency modulation, and phase inversion of each echo relative to the previous one due to the reflective boundary conditions. The amplitude of subsequent echoes (both in the frequency and in the time domain) depends strongly on the reflectivity \mathcal{R} . When $\mathcal{R} \approx 1$ the echo signal has amplitude and energy significantly larger than those of the ordinary BH ringdown. This suggests that GW echoes in certain models might be detectable even when the ringdown is not.

Using a Fisher analysis, we have then estimated the statistical errors on the template parameters for a post-merger GW detection with current and future interferometers. Interestingly, for signals in the optimal frequency window, the statistical errors at a given SNR depend only mildly on the detector’s sensitivity curve.

Our analysis suggests that ECO models with $\mathcal{R} \approx 1$ can be detected or ruled out even with aLIGO/Virgo (for events with $\rho \gtrsim 8$ in the ringdown phase) at 5σ confidence level. The same event might allow us to probe values of the reflectivity as small as $\mathcal{R} \approx 0.8$ roughly at 2σ confidence level. Overall, the detectability of the echoes is independent of the parameter d in the large- d limit (i.e., for ultracompact objects).

ECOs with $\mathcal{R} = 1$ are ruled out by the ergoregion instability [36, 48] and by the absence of GW stochastic background in LIGO O1 [16]. Excluding/detecting echoes with smaller values of the reflectivity (for which the ergoregion instability is absent [36]) will require SNRs in the post-merger phase of $\mathcal{O}(100)$. This will be achievable only with third-generation detectors (ET and Cosmic Explorer) and with the space-mission LISA.

Although our analysis is preliminary, we believe that our results already indicate that interesting constraints on (or detection of) quantum-dressed ECOs are within

reach with current (and especially future) interferometers.

Extensions of this work are manifold. A template valid for the spinning case is underway. This case is particularly interesting, not only because merger remnants are spinning, but also because of the rich phenomenology of spinning horizonless objects, which might undergo various types of instabilities [25, 36, 45, 48, 50–52]. In particular, due to superradiance [45] and to the ergoregion instability [25, 53], the echo signal will grow in time over a timescale $\tau_{\text{ergoregion}}$ which is generically much longer than $\tau_{\text{echo}} \sim d$. Another natural extension concerns the role of the boundary conditions at the surface for gravitational perturbations [54] – especially in the spinning case – and on model-independent ways to describe the interior of the object in case of partial absorption (cf., e.g., Ref. [16]).

Furthermore, a more realistic model could be obtained by reprocessing the full form of Z_{BH}^+ containing both the ringdown and the late-merger signal [i.e., using the template (24)], or using a superposition of QNMs. This extension will be particularly important to compare our template (constructed within perturbation theory and therefore strictly speaking valid only for weak sources) with the post-merger signal of coalescences forming an “echoing” ultracompact horizonless object. Unfortunately, numerical simulations of these systems are currently unavailable, but we envisage that a comparison between analytical and numerical waveforms will eventually follow a path similar to what done in the past for the matching of ringdown templates with numerical-relativity waveforms (see, e.g., Ref. [55]).

Another interesting prospect is to analyze the prompt-ringdown signal and the late-time one separately. Since the prompt response is universal [1], it could be used to infer the mass and the spin of the final object, thus making it easier to extract the echo parameters from the post-merger phase at late times. Finally, it should be straightforward to extend our analysis to complex and (possibly) frequency-dependent values of \mathcal{R} and to include two polarizations. These analyses and other applications are left for future work.

ACKNOWLEDGMENTS

The authors acknowledge interesting discussion with the members of the GWIC-3G-XG/NRAR working group, the financial support provided under the European Union’s H2020 ERC, Starting Grant agreement no. DarkGRA–757480, and networking support by the COST Action CA16104. PP acknowledges the kind hospitality of the Universitat de les Illes Balears, where this work has been finalized.

Appendix A: Transfer function in the geometrical optics approximation

In this appendix we derive Eqs. (6) and (22) using a geometrical optics analogy. For simplicity, we fix the position of the peak of the potential at $x = 0$ rather than at $x = x_m$. We replace the reflective surface and the light ring with two partially reflective mirrors, respectively left (L) at $x = -d < 0$ and right (R) at $x = 0$, and each Fourier component of the perturbation with a light ray represented by a complex number. We are left with a Fabry-Perot interferometer that can be studied as in optics textbooks. In the main text we consider a source $\tilde{S}(\omega, x) = C(\omega)\delta(x - x_s)$, which is symmetric with respect to the direction of propagation. This will produce two rays originating at $x_s = -d + \ell$, one going to the left and the other to the right with the same amplitude $C(\omega)$. The left-going ray travels toward L acquiring a phase $e^{i\omega\ell}$, is reflected at L gaining a factor \mathcal{R} , and then acquires an extra phase $e^{i\omega\ell}$ before joining the first ray in their common future evolution. The two rays then travel toward R with a total amplitude $C(\omega)(1 + \mathcal{R}e^{2i\omega\ell})$. Travelling to R they gather a phase $e^{i\omega(d-\ell)}$. Upon impinging on R the wave is partly reflected and partly transmitted. The transmitted part gains a factor $\mathcal{T}_{\text{BH}}(\omega)$ and then travels to $+\infty$. The reflected wave gains a factor $\mathcal{R}_{\text{BH}}(\omega)$ and travels from R to L, acquiring an extra phase $e^{i\omega d}$, and keeps repeating the same steps already described. Thus, the waveform can be written as

$$\begin{aligned} \tilde{\Psi}(\omega, x \rightarrow \infty) &\sim C(\omega)e^{i\omega(d-\ell)}\mathcal{T}_{\text{BH}}(\omega)(1 + \mathcal{R}e^{2i\omega\ell})e^{i\omega x} \\ &= \tilde{Z}_{\text{BH}}^+(\omega)(1 + \mathcal{R}e^{2i\omega\ell})e^{i\omega x}, \end{aligned} \quad (\text{A1})$$

where

$$\tilde{Z}_{\text{BH}}^+(\omega) = C(\omega)e^{i\omega(d-\ell)}\mathcal{T}_{\text{BH}}(\omega), \quad (\text{A2})$$

is the BH response, corresponding to the amplitude of the right-going wave in Eq. (A1) when $\mathcal{R} = 0$.

To compute \tilde{Z}_{BH}^- we consider the amplitude of the total left-going signal near $x \sim -d$ and set $\mathcal{R} = 0$:

$$\tilde{Z}_{\text{BH}}^- = [C(\omega)e^{i\omega\ell} + C(\omega)\mathcal{R}_{\text{BH}}(\omega)e^{2i\omega d}e^{-i\omega\ell}]e^{-i\omega d}, \quad (\text{A3})$$

where we added the phase factor $e^{i\omega d}$ to take into account the convention about the origin of the asymptotic behaviors. Considering Eqs. (A2) and (A3) we recover Eq. (22) for $x_m = 0$ (i.e. $x_0 = -d$).

It is now straightforward to calculate the signal at infinity as a sum of the transmitted waves at R:

$$\begin{aligned} \tilde{Z}^+(\omega) &= (1 + \mathcal{R}e^{2i\omega\ell})Z_{\text{BH}}^+(\omega) \left[1 + \sum_{n=1}^{\infty} (\mathcal{R}\mathcal{R}_{\text{BH}}e^{2i\omega d})^n \right] \\ &= (1 + \mathcal{R}e^{2i\omega\ell})Z_{\text{BH}}^+(\omega) \frac{1}{1 - \mathcal{R}\mathcal{R}_{\text{BH}}e^{2i\omega d}}, \end{aligned} \quad (\text{A4})$$

which gives Eqs. (6) and (9) when \tilde{Z}_{BH}^- is given by Eq. (22). The above argument can also be extended to generic sources [42].

Appendix B: The functions \mathcal{T}_{BH} , \mathcal{R}_{BH} and \mathcal{K} in the analytical approximation

Here we compare our approximate analytical results with the exact numerical ones as computed by Mark et al. [19]. Note that our definition of the tortoise coordinate x differs by a constant term, $-2M \log 2$, relative to the one adopted in Ref. [19]. For the purpose of comparison, only in this section we have rescaled $x_0 \rightarrow x_0 - 2M \log 2$ to agree with the definition of Ref. [19].

In the left panel of Fig. 9 we compare the approximate analytical functions $\mathcal{T}_{\text{BH}}(\omega)$, $\mathcal{R}_{\text{BH}}(\omega)$ with their exact numerical behavior. This plot reproduces Fig. 3 in Ref. [19]. We also compare the functions

$$\mathcal{K}_n(\omega) = (\mathcal{T}_{\text{BH}}\mathcal{R})(\mathcal{R}_{\text{BH}}\mathcal{R})^{n-1}e^{-2i\omega x_0}, \quad (\text{B1})$$

for different values of n with their numerical counterparts. Note that we show the absolute value of \mathcal{K}_n and normalize it by \mathcal{R}^n ; with this choice, the result is independent of x_0 and \mathcal{R} .

In the right panel of Fig. 9 we present the analytical transfer function $\mathcal{K}(\omega)$ [cf. Eq. (18)] for different values of x_0 and \mathcal{R} , and compare it with its exact numerical expression. This plot reproduces Fig. 13 in Ref. [19]. We note that, while the agreement of the analytical approximation for the full transfer function $\mathcal{K}(\omega)$ is very good (the differences between numerics and analytics are barely distinguishable in the right panel of Fig. 9), the single terms $\mathcal{K}_n(\omega)$ are less accurate.

Note also the appearance of more narrow resonances as $|x_0| \gg M$, some of them not being resolved in Fig. 13 of Ref. [19]. These resonances correspond to the long-lived QNMs of the ECO: their separation is $\sim \pi/d$ and their narrow width is associated with the small imaginary part of the quasi-bound modes [25, 45].

For example, Eq. (10) implies Dirichlet or Neumann boundary conditions at $x = x_0$ for $\mathcal{R} = -1$ or $\mathcal{R} = 1$, respectively. In this case, the normal modes of a cavity of width d at low frequency ($\mathcal{T}_{\text{BH}} \approx 0$) read

$$\omega_D \sim \frac{p\pi}{d}, \quad \omega_N \sim \frac{(2p+1)\pi}{2d}, \quad (\text{B2})$$

for Dirichlet and Neumann boundary conditions, respectively, and where p is an integer.

In the right panel of Fig. 9 we also show the case of a wormhole, for which $\mathcal{R} = \mathcal{R}_{\text{BH}}e^{-2i\omega x_0}$ [19]. Although marginally visible in Fig. 9, in this case $\mathcal{K}(\omega)$ does not vanish as $\omega \rightarrow 0$. This behavior holds generically whenever $\mathcal{R}(\omega \approx 0) = -1 + \mathcal{O}(\omega)$. Indeed, in this case we get

$$\mathcal{K}(0) = \frac{\pi \operatorname{sech}\left(\frac{\pi\omega_R}{\alpha}\right)}{H_{-i\frac{\omega_R}{\alpha}-\frac{1}{2}} + H_{i\frac{\omega_R}{\alpha}-\frac{1}{2}} - \alpha(2d + i\mathcal{R}'(0))}, \quad (\text{B3})$$

with $H_n = F(n+1) + \gamma_E$, F is the digamma function and γ_E is the Euler-Mascheroni constant. As ex-

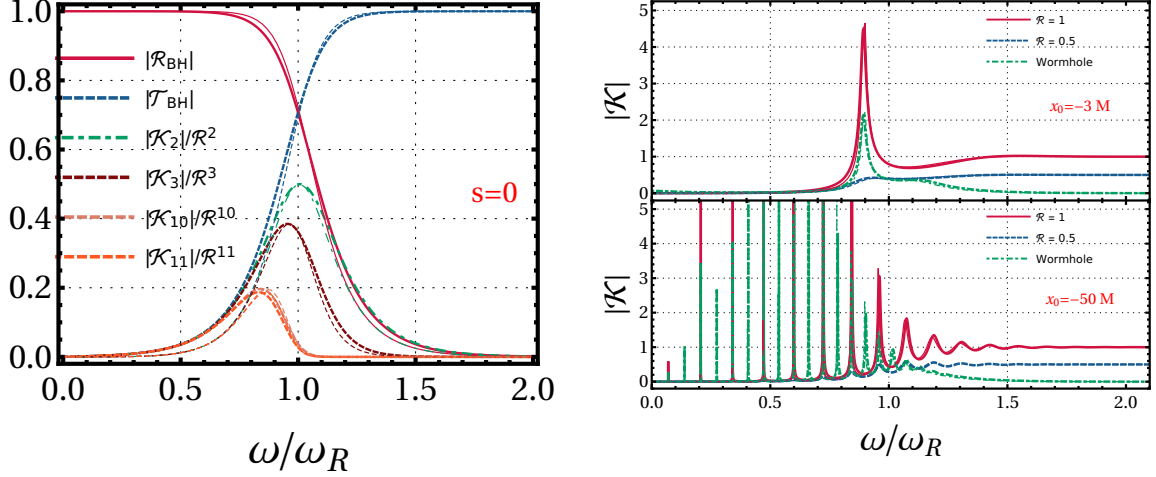


FIG. 9. Left panel: the functions $\mathcal{T}_{\text{BH}}(\omega)$ and $\mathcal{R}_{\text{BH}}(\omega)$ as computed in our analytical approximation, together with the functions $\mathcal{K}_n(\omega)$ defined in Eq. (B1). Thin curves correspond to the exact numerical results with the same color and linestyle. Right panel: same as the left panel but for the transfer function $\mathcal{K}(\omega)$ in various cases. Note that the agreement for the full transfer function $\mathcal{K}(\omega)$ is better than that for the individual \mathcal{K}_n .

pected $\mathcal{K}(0) \rightarrow 0$ as $d \rightarrow \infty$ (assuming no cancellations occur due to the $\mathcal{R}'(0)$ term) but is otherwise finite. By differentiating $\mathcal{R}(\omega) = \mathcal{R}^*(-\omega)$ we see that $\mathcal{R}'(0)$ is purely imaginary, and therefore $\mathcal{K}(0)$ is purely real, in accordance with Eq. (11). In the wormhole case, $\mathcal{R}'_{\text{WH}}(0) = \mathcal{R}'_{\text{BH}}(0) - 2id$, and we obtain

$$\mathcal{K}(0) = \frac{\pi \operatorname{sech}(\frac{\pi\omega_R}{\alpha})/2}{H_{-i\frac{\omega_R}{\alpha}-\frac{1}{2}} + H_{i\frac{\omega_R}{\alpha}-\frac{1}{2}} - 2\alpha d}. \quad (\text{B4})$$

Appendix C: Frequency-domain analytical template for a source localized in a generic position

Equation (24) in the main text was derived assuming a source localized near the surface at $x_s \approx x_0$. It is possible

to extend this result to a source localized at any x_s [42]. From the analytical solution of the homogeneous problem [Eq. (14)], it is possible to derive the two independent solutions $\tilde{\Psi}_{\pm}$ that appear in the definition (7). If $\tilde{S} = C(\omega)\delta(x - x_s)$, then

$$Z_{\text{BH}}^-(\omega) = Z_{\text{BH}}^+(\omega) \frac{\tilde{\Psi}_+(x = x_s, \omega)}{\tilde{\Psi}_-(x = x_s, \omega)}, \quad (\text{C1})$$

which is again valid for any function $C(\omega)$ characterizing the source. It is now straightforward to obtain the generalization of Eq. (24):

$$\tilde{Z}^+(\omega) = Z_{\text{BH}}^+(\omega) (1 - \mathcal{G}\mathcal{R}e^{2i\omega d}), \quad (\text{C2})$$

where

$$\mathcal{G} = \frac{\pi \sinh[\frac{\pi\omega}{\alpha}] \Upsilon P_{\frac{i\omega}{\omega_R} - \frac{1}{2}}^{\frac{i\omega}{\alpha}}(z)}{(\pi + e^{2id\omega} \mathcal{R} \cosh[\frac{\pi\omega_R}{\alpha}] \Upsilon) \left(\pi \sinh[\frac{\pi(\omega+\omega_R)}{\alpha}] P_{\frac{i\omega}{\omega_R} - \frac{1}{2}}^{\frac{i\omega}{\alpha}}(z) - 2i \cosh[\frac{\pi(\omega+\omega_R)}{\alpha}] Q_{\frac{i\omega}{\omega_R} - \frac{1}{2}}^{\frac{i\omega}{\alpha}}(z) \right)}, \quad (\text{C3})$$

Υ is defined in Eq. (17), $z = -\tanh(\alpha\Delta)$, and $\Delta = x_m - x_s$. Note that $\Delta = d$ when $x_s = x_0$ and that $\Delta > 0$ for a source localized in the cavity, whereas $\Delta < 0$ for a source localized outside the photon-sphere. Equation (C2) reduces to Eq. (24) when $\Delta = d \gg M$, as expected.

Appendix D: A toy model for the dependence on d of the Fisher matrix

In this appendix we give an analytical argument showing that the absolute errors on our template's parameters computed through the Fisher matrix are independent of d in the large- d limit.

We start by modeling the echo signal in the time domain as

$$\Psi(t) = \sum_{n=0}^{\infty} g(t - 2nd)e^{-n\gamma}, \quad (\text{D1})$$

where d is the width of the cavity, γ is a dumping factor, and g is a generic function. Taking the Fourier transform of Eq. (D1), we obtain

$$\tilde{\Psi}(\omega) = \sum_{n=0}^{\infty} e^{-n\gamma} \int_{-\infty}^{+\infty} \frac{dt}{\sqrt{2\pi}} g(t - 2nd)e^{i\omega t}. \quad (\text{D2})$$

By making the change of variable $t' = t - 2nd$, we get

$$\begin{aligned} \tilde{\Psi}(\omega) &= \sum_{n=0}^{\infty} e^{-n\gamma} \int_{-\infty}^{+\infty} \frac{dt'}{\sqrt{2\pi}} g(t')e^{i\omega t'} e^{2i\omega nd} \\ &= \sum_{n=0}^{\infty} e^{-n\gamma} e^{2i\omega nd} \int_{-\infty}^{+\infty} \frac{dt}{\sqrt{2\pi}} g(t)e^{i\omega t} \\ &= \tilde{g}(\omega)A(\omega; \gamma, d), \end{aligned} \quad (\text{D3})$$

where

$$A(\omega; \gamma, d) = \frac{1}{1 - e^{-(\gamma - 2i\omega d)}}. \quad (\text{D4})$$

We notice that $A(\omega; \gamma, d)$ has the following properties

$$\begin{aligned} \lim_{\frac{d}{d_c} \rightarrow \infty} \int_{-\infty}^{+\infty} f(\omega)A(\omega; \gamma, d)d\omega &= c_1(\gamma) \int_{-\infty}^{+\infty} f(\omega)d\omega, \\ \lim_{\frac{d}{d_c} \rightarrow \infty} \frac{\partial}{\partial \gamma} \int_{-\infty}^{+\infty} f(\omega)A(\omega; \gamma, d)d\omega &= c_2(\gamma) \int_{-\infty}^{+\infty} d\omega f(\omega), \\ \lim_{\frac{d}{d_c} \rightarrow \infty} \frac{\partial}{\partial d} \int_{-\infty}^{+\infty} d\omega f(\omega)A(\omega; \gamma, d) &= c_3(\gamma) \int_{-\infty}^{+\infty} d\omega f(\omega)\omega, \end{aligned}$$

where $\sim 1/d_c$ is the characteristic scale of variations of the function $f(\omega)$. From the above relations, it follows immediately that the absolute statistical errors derived from the Fisher matrix are independent of d when $d \gg d_c$.

In our specific case, the typical frequency scale of the function $\tilde{g}(\omega)$ is the BH ringdown frequency, $\omega_R \approx 0.37/M$. Thus the large- d limit is achieved when

$$\frac{0.37}{M} \gg \frac{\pi}{d}, \quad (\text{D5})$$

which requires $d \gg 10M$. For larger values of d , we expect that the relative errors such as $\Delta\mathcal{R}/\mathcal{R}$ to be independent on d , whereas $\Delta d/d \sim 1/d$. The numerical results presented in the main text support this expectation when $d \gg 50M$.

-
- [1] V. Cardoso, E. Franzin, and P. Pani, “Is the gravitational-wave ringdown a probe of the event horizon?,” *Phys. Rev. Lett.* **116** no. 17, (2016) 171101, [arXiv:1602.07309 \[gr-qc\]](#). [Erratum: *Phys. Rev. Lett.*117,no.8,089902(2016)].
- [2] V. Cardoso, S. Hopper, C. F. B. Macedo, C. Palenzuela, and P. Pani, “Gravitational-wave signatures of exotic compact objects and of quantum corrections at the horizon scale,” *Phys. Rev.* **D94** no. 8, (2016) 084031, [arXiv:1608.08637 \[gr-qc\]](#).
- [3] V. Ferrari and K. D. Kokkotas, “Scattering of particles by neutron stars: Time evolutions for axial perturbations,” *Phys. Rev.* **D62** (2000) 107504, [arXiv:gr-qc/0008057 \[gr-qc\]](#).
- [4] P. Pani and V. Ferrari, “Comment on gravitational-wave echoes from neutron-star binary coalescences,” [arXiv:1804.01444 \[gr-qc\]](#).
- [5] V. Cardoso and P. Pani, “Tests for the existence of horizons through gravitational wave echoes,” *Nat. Astron.* **1** (2017) 586–591, [arXiv:1709.01525 \[gr-qc\]](#).
- [6] V. Cardoso and P. Pani, “The observational evidence for horizons: from echoes to precision gravitational-wave physics,” [arXiv:1707.03021 \[gr-qc\]](#).
- [7] J. Abedi, H. Dykaar, and N. Afshordi, “Echoes from the Abyss: Tentative evidence for Planck-scale structure at black hole horizons,” *Phys. Rev.* **D96** no. 8, (2017) 082004, [arXiv:1612.00266 \[gr-qc\]](#).
- [8] R. S. Conklin, B. Holdom, and J. Ren, “Gravitational wave echoes through new windows,” [arXiv:1712.06517 \[gr-qc\]](#).
- [9] G. Ashton, O. Birnholtz, M. Cabero, C. Capano, T. Dent, B. Krishnan, G. D. Meadors, A. B. Nielsen, A. Nitz, and J. Westerweck, “Comments on: ”Echoes from the abyss: Evidence for Planck-scale structure at black hole horizons,”” [arXiv:1612.05625 \[gr-qc\]](#).
- [10] J. Abedi, H. Dykaar, and N. Afshordi, “Echoes from the Abyss: The Holiday Edition!,” [arXiv:1701.03485 \[gr-qc\]](#).
- [11] J. Westerweck, A. Nielsen, O. Fischer-Birnholtz, M. Cabero, C. Capano, T. Dent, B. Krishnan,

- G. Meadors, and A. H. Nitz, “Low significance of evidence for black hole echoes in gravitational wave data,” [arXiv:1712.09966](https://arxiv.org/abs/1712.09966) [gr-qc].
- [12] J. Abedi, H. Dykaar, and N. Afshordi, “Comment on: ”Low significance of evidence for black hole echoes in gravitational wave data”,” [arXiv:1803.08565](https://arxiv.org/abs/1803.08565) [gr-qc].
- [13] **Virgo, LIGO Scientific** Collaboration, B. P. Abbott *et al.*, “GW170817: Observation of Gravitational Waves from a Binary Neutron Star Inspiral,” *Phys. Rev. Lett.* **119** no. 16, (2017) 161101, [arXiv:1710.05832](https://arxiv.org/abs/1710.05832) [gr-qc].
- [14] J. Abedi and N. Afshordi, “Echoes from the Abyss: A highly spinning black hole remnant for the binary neutron star merger GW170817,” [arXiv:1803.10454](https://arxiv.org/abs/1803.10454) [gr-qc].
- [15] S. M. Du and Y. Chen, “Searching for near-horizon quantum structures in the binary black-hole stochastic gravitational-wave background,” [arXiv:1803.10947](https://arxiv.org/abs/1803.10947) [gr-qc].
- [16] E. Barausse, R. Brito, V. Cardoso, I. Dvorkin, and P. Pani, “The stochastic gravitational-wave background in the absence of horizons,” [arXiv:1805.08229](https://arxiv.org/abs/1805.08229) [gr-qc].
- [17] K. W. Tsang, M. Rollier, A. Ghosh, A. Samajdar, M. Agathos, K. Chatziioannou, V. Cardoso, G. Khanna, and C. Van Den Broeck, “A morphology-independent data analysis method for detecting and characterizing gravitational wave echoes,” [arXiv:1804.04877](https://arxiv.org/abs/1804.04877) [gr-qc].
- [18] H. Nakano, N. Sago, H. Tagoshi, and T. Tanaka, “Black hole ringdown echoes and howls,” *PTEP* **2017** no. 7, (2017) 071E01, [arXiv:1704.07175](https://arxiv.org/abs/1704.07175) [gr-qc].
- [19] Z. Mark, A. Zimmerman, S. M. Du, and Y. Chen, “A recipe for echoes from exotic compact objects,” *Phys. Rev. D* **96** no. 8, (2017) 084002, [arXiv:1706.06155](https://arxiv.org/abs/1706.06155) [gr-qc].
- [20] A. Maselli, S. H. Volkel, and K. D. Kokkotas, “Parameter estimation of gravitational wave echoes from exotic compact objects,” *Phys. Rev. D* **96** no. 6, (2017) 064045, [arXiv:1708.02217](https://arxiv.org/abs/1708.02217) [gr-qc].
- [21] P. Bueno, P. A. Cano, F. Goelen, T. Hertog, and B. Verhocke, “Echoes of Kerr-like wormholes,” *Phys. Rev. D* **97** no. 2, (2018) 024040, [arXiv:1711.00391](https://arxiv.org/abs/1711.00391) [gr-qc].
- [22] Y.-T. Wang, Z.-P. Li, J. Zhang, S.-Y. Zhou, and Y.-S. Piao, “Are gravitational wave ringdown echoes always equal-interval?,” [arXiv:1802.02003](https://arxiv.org/abs/1802.02003) [gr-qc].
- [23] M. R. Correia and V. Cardoso, “Characterization of echoes: a Dyson-series representation of individual pulses,” [arXiv:1802.07735](https://arxiv.org/abs/1802.07735) [gr-qc].
- [24] Q. Wang and N. Afshordi, “Black Hole Echology: The Observer’s Manual,” [arXiv:1803.02845](https://arxiv.org/abs/1803.02845) [gr-qc].
- [25] V. Cardoso, L. C. B. Crispino, C. F. B. Macedo, H. Okawa, and P. Pani, “Light rings as observational evidence for event horizons: long-lived modes, ergoregions and nonlinear instabilities of ultracompact objects,” *Phys. Rev. D* **90** no. 4, (2014) 044069, [arXiv:1406.5510](https://arxiv.org/abs/1406.5510) [gr-qc].
- [26] **LIGO** Collaboration, D. Shoemaker, “Advanced ligo anticipated sensitivity curves,” Tech. Rep. T0900288-v3, 2010. <https://dcc.ligo.org/LIGO-T0900288/public>.
- [27] M. Punturo *et al.*, “The Einstein Telescope: A third-generation gravitational wave observatory,” *Class. Quant. Grav.* **27** (2010) 194002.
- [28] S. Dwyer, D. Sigg, S. W. Ballmer, L. Barsotti, N. Mavalvala, and M. Evans, “Gravitational wave detector with cosmological reach,” *Phys. Rev. D* **91** (Apr, 2015) 082001. <https://link.aps.org/doi/10.1103/PhysRevD.91.082001>.
- [29] H. Audley, S. Babak, J. Baker, E. Barausse, P. Bender, E. Berti, P. Binetruy, M. Born, D. Bortoluzzi, J. Camp, C. Caprini, V. Cardoso, M. Colpi, J. Conklin, N. Cornish, C. Cutler, *et al.*, “Laser Interferometer Space Antenna,” *ArXiv e-prints* (Feb., 2017) , [arXiv:1702.00786](https://arxiv.org/abs/1702.00786) [astro-ph.IM].
- [30] **LIGO Scientific** Collaboration, B. P. Abbott *et al.*, “Exploring the Sensitivity of Next Generation Gravitational Wave Detectors,” *Class. Quant. Grav.* **34** no. 4, (2017) 044001, [arXiv:1607.08697](https://arxiv.org/abs/1607.08697) [astro-ph.IM].
- [31] R. Essick, S. Vitale, and M. Evans, “Frequency-dependent responses in third generation gravitational-wave detectors,” *Phys. Rev. D* **96** no. 8, (2017) 084004, [arXiv:1708.06843](https://arxiv.org/abs/1708.06843) [gr-qc].
- [32] S. Hild *et al.*, “Sensitivity Studies for Third-Generation Gravitational Wave Observatories,” *Class. Quant. Grav.* **28** (2011) 094013, [arXiv:1012.0908](https://arxiv.org/abs/1012.0908) [gr-qc].
- [33] G. Poschl and E. Teller, “Bemerkungen zur Quantenmechanik des anharmonischen Oszillators,” *Z. Phys.* **83** (1933) 143–151.
- [34] V. Ferrari and B. Mashhoon, “New approach to the quasinormal modes of a black hole,” *Phys. Rev. D* **30** (1984) 295–304.
- [35] <http://www.darkgra.org>.
- [36] E. Maggio, P. Pani, and V. Ferrari, “Exotic Compact Objects and How to Quench their Ergoregion Instability,” *Phys. Rev. D* **96** no. 10, (2017) 104047, [arXiv:1703.03696](https://arxiv.org/abs/1703.03696) [gr-qc].
- [37] S. Chandrasekhar, *The Mathematical Theory of Black Holes*. Oxford University Press, New York, 1983.
- [38] I. Novikov and V. Frolov, *Black Hole Physics*. Springer, 1989.
- [39] E. Berti, V. Cardoso, and A. O. Starinets, “Quasinormal modes of black holes and black branes,” *Class. Quantum Grav.* **26** (2009) 163001, [arXiv:0905.2975](https://arxiv.org/abs/0905.2975) [gr-qc].
- [40] E. W. Leaver, “Spectral decomposition of the perturbation response of the Schwarzschild geometry,” *Phys. Rev. D* **34** (1986) 384–408.
- [41] E. Berti, V. Cardoso, and C. M. Will, “On gravitational-wave spectroscopy of massive black holes with the space interferometer LISA,” *Phys. Rev. D* **73** (2006) 064030, [arXiv:gr-qc/0512160](https://arxiv.org/abs/gr-qc/0512160) [gr-qc].
- [42] A. Testa, “Master thesis, Sapienza University of Rome,”.
- [43] E. E. Flanagan and S. A. Hughes, “Measuring gravitational waves from binary black hole coalescences: 1. Signal-to-noise for inspiral, merger, and ringdown,” *Phys. Rev. D* **57** (1998) 4535–4565, [arXiv:gr-qc/9701039](https://arxiv.org/abs/gr-qc/9701039) [gr-qc].
- [44] E. Barausse, V. Cardoso, and P. Pani, “Can environmental effects spoil precision gravitational-wave astrophysics?,” *Phys. Rev. D* **89** no. 10, (2014) 104059, [arXiv:1404.7149](https://arxiv.org/abs/1404.7149) [gr-qc].
- [45] R. Brito, V. Cardoso, and P. Pani, “Superradiance,” *Lect. Notes Phys.* **906** (2015) pp.1–237, [arXiv:1501.06570](https://arxiv.org/abs/1501.06570) [gr-qc].
- [46] M. Vallisneri, “Use and abuse of the Fisher information matrix in the assessment of gravitational-wave

- parameter-estimation prospects,” *Phys. Rev.* **D77** (2008) 042001, [arXiv:gr-qc/0703086](#) [GR-QC].
- [47] K. Chatziioannou, N. Cornish, A. Klein, and N. Yunes, “Detection and parameter estimation of gravitational waves from compact binary inspirals with analytical double-precessing templates,” *Phys. Rev. D* **89** (May, 2014) 104023. <https://link.aps.org/doi/10.1103/PhysRevD.89.104023>.
- [48] V. Cardoso, P. Pani, M. Cadoni, and M. Cavaglia, “Instability of hyper-compact Kerr-like objects,” *Class. Quant. Grav.* **25** (2008) 195010, [arXiv:0808.1615](#) [gr-qc].
- [49] **LIGO Scientific Collaboration and Virgo Collaboration** Collaboration, B. P. Abbott *et al.*, “Observation of gravitational waves from a binary black hole merger,” *Phys. Rev. Lett.* **116** (Feb, 2016) 061102. <https://link.aps.org/doi/10.1103/PhysRevLett.116.061102>.
- [50] J. L. Friedman, “Ergosphere instability,” *Communications in Mathematical Physics* **63** (Oct., 1978) 243–255.
- [51] G. Moschidis, “A proof of Friedman’s ergosphere instability for scalar waves,” [arXiv:1608.02035](#) [math.AP].
- [52] V. Cardoso, P. Pani, M. Cadoni, and M. Cavaglia, “Ergoregion instability of ultracompact astrophysical objects,” *Phys. Rev.* **D77** (2008) 124044, [arXiv:0709.0532](#) [gr-qc].
- [53] R. Vicente, V. Cardoso, and J. C. Lopes, “The Penrose process, superradiance and ergoregion instabilities,” [arXiv:1803.08060](#) [gr-qc].
- [54] R. H. Price and G. Khanna, “Gravitational wave sources: reflections and echoes,” *Class. Quant. Grav.* **34** no. 22, (2017) 225005, [arXiv:1702.04833](#) [gr-qc].
- [55] A. Buonanno, G. B. Cook, and F. Pretorius, “Inspirals, merger and ring-down of equal-mass black-hole binaries,” *Phys. Rev.* **D75** (2007) 124018, [arXiv:gr-qc/0610122](#) [gr-qc].